

# Pore-end effects on adsorption hysteresis in cylindrical and slitlike pores

Aphrodite Papadopoulou and Frank van Swol  
*Department of Chemical Engineering, University of Illinois, Urbana, Illinois 61801*

Umberto Marini Bettolo Marconi  
*Dipartimento di Matematica e Fisica, Università di Camerino, via Madonna della Carceri, 62032  
Camerino, Italy Matematica e Fisica, Università di Camerino, Italy*

(Received 22 April 1992; accepted 22 May 1992)

We present grand canonical and canonical simulation results for the adsorption hysteresis in cylindrical and slitlike pores. Simulations for cylindrical symmetry were carried out for a continuous potential model, whereas the lattice gas was used to investigate the slitlike pores. In particular, we have studied the effects of pore ends on pore filling and pore emptying mechanism. We find that while the pore filling is unaffected, pore emptying is very sensitive to the presence of pore ends. Our findings confirm earlier lattice gas density functional theory results and indicate that fluctuations do not basically alter the mean field picture.

## I. INTRODUCTION

In recent years significant progress has been made in understanding fluid behavior in narrow pores. An important phenomenon connected with this behavior is capillary condensation of the adsorbed phase and the adsorption hysteresis, which usually accompanies it. That is, the gaslike fluid confined in the pore condenses at an undersaturated bulk pressure (or equivalently chemical potential,  $\mu$ ) forming a liquidlike phase. However, in certain pore geometries, when the bulk pressure is decreased the fluid jumps back to the gaslike state at a pressure significantly lower than the condensation pressure, thus producing a hysteresis loop.

A variety of methods have been employed to locate the capillary condensation transition and understand the origin of the adsorption hysteresis. Two schools of thought exist: one connects hysteresis to metastable equilibrium gaslike and liquidlike states ultimately due to the geometry of a single pore, and the other links hysteresis to the interconnectivity of pores.<sup>1</sup> The latter scheme, pursued by Mason, assumes no hysteresis in a single pore and ascribes the origin of the experimentally observed hysteresis to a pore blocking effect, which is likely to be present in a system of interconnected pores, especially when the interconnected pores are of widely different diameters.<sup>2</sup> Only recently has it become possible to experiment on a medium of well-defined pores, a cluster of pores with sharp pore size distribution which implies little pore blocking.<sup>3</sup> Hysteresis was observed, thus providing evidence for the importance of the individual pore hysteresis.

Molecular simulation methods as well as density functional theory (DFT) have been employed to study fluid behavior in a single pore. Typically, idealized pore structures, such as periodic cylindrical and slitlike pores, have been considered to investigate phase transitions of one component as well as mixtures of fluids. In the simulations one assumes a pore of a certain length and applies periodic boundaries (PBC) to its ends, such that the resulting total structure is topologically a torus of finite length. We shall refer to this kind of pore as a PBC pore and note that it can

often be regarded as an infinite pore. The traditional DFT calculations consider the density to vary in one direction only, the latter being the direction perpendicular to the pore walls in a slitlike pore, or the radial direction in the case of a cylindrical pore. Hence, DFT is most closely mimicked by a simulation of a PBC pore. The local density approximation functional theory gave a first insight into the phase behavior of the fluid in a PBC pore and later the more refined version, the smoothed density (or nonlocal) approximation, produced an accurate description of the structure of the fluid inside the pore.<sup>4,5</sup> Peterson and Gubbins<sup>6</sup> used both mean field theory (MFT) and grand canonical Monte Carlo simulation (GCMC) for a PBC cylindrical pore, and observed a hysteresis loop with extended metastable branches. The metastable liquidlike branch smoothly extended to values below the coexistence  $\mu$  followed by an abrupt jump to the gaslike branch without exhibiting a rounded knee as present in some experimental work. Heffelfinger *et al.*<sup>7</sup> studied the same system described in Ref. 6 by using molecular dynamics (MD) in a canonical ensemble, i.e., using a constant number of particles, and observed the coexistence of two phases separated by hemispherical menisci. The two methods predicted an almost identical coexistence chemical potential for the PBC cylindrical pore. The above results strongly indicate the existence of hysteresis in a single periodic pore and thus one may link the experimentally observed adsorption hysteresis not only to the interconnectivity of pores and the pore blocking effects but also to the individual pore geometry. On the other hand, Schoen *et al.*<sup>8</sup> have argued that the observation of hysteresis in molecular simulations is only due to computer time limitation (or equivalently the length of the Markov chains). This is a well-known observation<sup>9</sup> which indicates that the concept of metastability is only meaningful when one quotes observation times. Metastable states exist because of the existence of separate regions in phase space which are poorly connected. These poor connections reflect the nucleation barriers which, given infinite time (i.e., complete sampling of phase space) will always be overcome. In fact, molecular simulations closely mimic the experiments in that both

show metastability and thus hysteresis for finite observation times and in both cases barriers are present to preclude the spontaneous formation of the new phase when the phase transition is approached.

In a porous medium, the pores are not infinitely long nor always toroidal, which are features of the systems simulated in Refs. 6 and 7. The effects of the finite pore size and the presence of pore ends on the hysteresis were first investigated by Marini Bettolo Marconi and van Swol<sup>10</sup> who used the DFT method for both a PBC and a finite slitlike pore. Here, by finite pore we refer to a pore where the system consists of the pore and reservoirs of bulk fluid near its ends. The PBC pore produced an adsorption-desorption loop with extended metastable liquidlike and gaslike branches. In the case of the finite pore the authors observed hysteresis associated with the formation of concave menisci at the pore ends. The desorption branch rounds off and rapidly starts dropping at a pressure extremely close to the transition. The transition chemical potential is just inside the loop and at a value slightly larger than that for the infinite pore. The adsorption branch remains virtually the same for both systems. The main effect of the pore ends lies in the formation of an interface in the shape of a meniscus at the pore ends, while the effect of the finite size results in a mere shift of the hysteresis loop which forces the location of the actual transition to slightly larger values of  $\mu$  as the length of the pore decreases.

The major shortcoming of the DFT is that it uses a mean field approximation which neglects (or mistreats) the effect of fluctuations. The influence of the fluctuations can be assessed by performing molecular simulations. In this paper, we compare the results of simulations of a continuous simple fluid for a PBC pore with the results of grand canonical Monte Carlo (GCMC) for a finite sized cylindrical pore. We focus on the effects of the pore ends in the system and examine the structure of the fluid inside the pore. We also report the results of lattice gas simulations on PBC and finite slitlike pores and compare our results with the predictions of Marini Bettolo Marconi and van Swol.<sup>10</sup>

## II. SIMULATIONS

### A. Cylindrical pores

In the simulation of adsorption-desorption phenomena in a cylindrical pore we used the grand canonical ensemble (fixed chemical potential  $\mu$ , volume  $V$ , and temperature  $T$ ). For the fluid-fluid interactions we used the cut-and-shifted Lennard-Jones (LJ) potential,

$$\Phi_{cs}(r) = \begin{cases} \Phi_{LJ}(r) - \Phi_{LJ}(r_c) & \text{if } r \leq r_c \\ 0 & \text{if } r > r_c \end{cases}, \quad (1)$$

where  $r_c = 2.5\sigma$  is the cutoff distance and the LJ potential is given by

$$\Phi_{LJ}(r) = 4\epsilon \left[ \left( \frac{\sigma}{r} \right)^{12} - \left( \frac{\sigma}{r} \right)^6 \right], \quad (2)$$

where  $\epsilon$  is the potential well depth and  $\sigma$  the interparticle distance at which the potential crosses zero.

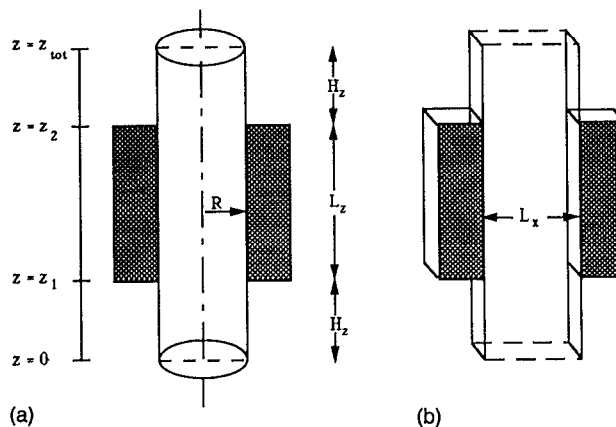


FIG. 1. Schematic diagram of the pore system [(a) cylindrical and (b) slitlike pore].  $L_z$  and  $H_z$  are the lengths of the pore and the reservoirs, respectively.  $R$  is the cylindrical pore radius and  $L_x$  the wall-to-wall distance in the slitlike pore. Periodic conditions are applied along the  $z$  direction and in the case of the slitlike pore along the  $y$  direction as well.

Following previous simulations,<sup>6,7</sup> the wall-fluid potential was taken to be a one-body potential found after the integration of the *full* LJ potential over the volume of the solid. For the case of an infinitely long pore

$$V_{\text{pore}}(r) = \rho_s \int_{\text{solid}} dr' \Phi_{LJ}(|r - r'|) \quad (3)$$

where  $r$  is the radial distance from the axis of the cylindrical pore and  $\rho_s$  is the density of the solid wall. The pore radius  $R$ , is defined to be the radius where  $V_{\text{pore}}(r)$  diverges. The parameters chosen were  $\epsilon_{fw}/\epsilon = 1.277$ ,  $\sigma_{fw}/\sigma = 1.094$ , and  $\rho_s/\sigma^3 = 0.988$  where the fw subscript denotes a fluid-wall potential parameter.<sup>6</sup>

We shall distinguish two kinds of simulations. The first we shall refer to as the PBC pore, where periodic boundary conditions are employed along the pore axis, which we shall take to be along the  $z$  direction. In the other type, which we shall refer to as a finite pore, bulk fluid reservoirs are attached to the pore ends. There is a variety of ways to implement a reservoir. For example, one can use a cubical box with PBC at the pore ends, each with one face connected to the pore end and the surrounding solid. This will necessarily expose some outer surface to the reservoir fluid. A somewhat simpler approach is to extend the cylindrical pore with two cylindrical hard wall reservoirs. Since hard walls are always completely dry and lead to extremely small disturbances of a low density reservoir fluid,<sup>11</sup> the properties of the confined reservoir fluid are essentially those of the bulk fluid. Hence, we adopted the cylindrical shape for the reservoirs, with hard wall potential,

$$\Phi_{hw}(r) = \begin{cases} 0 & r < R_c \\ \infty & r \geq R_c \end{cases}, \quad (4)$$

where  $R_c = R$  in our simulations. Note that the reservoir fluid is in thermal, chemical, and mechanical equilibrium with the adsorbed fluid inside the pore.

A schematic of the pore system is given in Fig. 1(a) and it shows the actual pore and the reservoirs. Periodic boundary conditions are applied along the  $z$  axis. It is im-

portant to note that although the periodic boundaries link the two reservoirs, they do not link opposite ends of the pore itself, so one clearly cannot view the system as a periodic pore of toroidal shape.

The total external field potential can be written as

$$V_{\text{ext}}(r,z) = \Phi_{\text{hw}}(r) + V_{\text{pore}}(r)\Theta(z-z_1)\Theta(z_2-z), \quad (5)$$

where  $\Theta$  denotes the Heaviside step function and  $z_1$  and  $z_2$  are the lower and the upper limit of the pore along the  $z$  direction, respectively [see Fig. 1(a)].

We used the GCMC implementation due to Adams.<sup>12,6</sup> Briefly, each step of this method consists of an attempted movement of a randomly chosen particle followed by either an attempted deletion of a randomly chosen particle or an attempted creation of a particle in a randomly chosen position inside the pore-reservoir system. We report our results as a function of the configurational potential  $\mu^{\text{conf}}$  defined as

$$\beta\mu^{\text{conf}} = \beta\mu - 3 \ln \Lambda/\sigma, \quad (6)$$

where  $\beta = 1/k_B T$  and  $k_B$  is the Boltzmann constant and  $\Lambda$  the De Broglie wavelength.

The capillary condensation transition for each pore length, whether the pore system includes reservoirs or not, can be found most directly by using an NVT Monte Carlo simulation (fixed number of particles,  $N$ , volume  $V$ , and temperature  $T$ ) with  $N$  suitably chosen to correspond to an intermediate configuration of coexisting liquid and vapor.<sup>7</sup> Such an approach, however, requires a measurement of the chemical potential. This was accomplished by using the potential distribution theorem (PDT) introduced first by Widom<sup>13,14</sup> and applied by Adams<sup>12</sup> to study bulk fluids and more recently by Heinbuch and Fischer<sup>15</sup> and Heffelfinger *et al.*<sup>7</sup> for inhomogeneous fluids. The PDT for an inhomogeneous fluid is given by:<sup>16</sup>

$$\beta\mu = 3 \ln(\Lambda/\sigma) + \ln[\rho(\underline{r})\sigma^3] - \ln\{\langle \exp[-\beta\Psi(\underline{r})] \rangle\}, \quad (7)$$

where  $\Psi(\underline{r})$  is the total potential energy felt by a test particle inserted at  $\underline{r}$ , due to all fluid particles and due to the external potential (i.e., the wall potential). The angular brackets denote an ensemble average. If the system is at equilibrium, the two logarithmic terms on the right hand side of Eq. (7), although each strongly dependent on  $\underline{r}$ , when added, should give a constant value. A problem of statistics arises when one samples close to the walls,  $r \simeq R$ . Here, both terms are very large and inaccurate and hence any small deviation from the true mean value introduces a large error in  $\mu$ . Thus, in practice, the probe volume for averaging  $\exp[-\beta\Psi(\underline{r})]$  and  $\rho(\underline{r})$  should be somewhat less than the pore system volume. The PDT is not only useful to locate the phase transition in an NVT simulation but it can also be used to test the constancy of the preset chemical potential during a  $\mu VT$  simulation. It is worthwhile to note that this information is easily acquired by monitoring and averaging the Boltzmann factor of each attempted creation, the conditionally created particle being a considered test particle.

## B. Slitlike pores

Following Marini Bettolo Marconi and van Swol<sup>10</sup> we used the three-dimensional lattice gas model to simulate capillary condensation of a lattice gas in a slitlike pore. The particles are allowed to occupy the lattice sites of a simple cubic lattice. Only nearest-neighbor interactions are present, the number of nearest neighbors in the bulk being equal to six. The Hamiltonian of this system is

$$H = -\epsilon \sum_{\langle ij \rangle} n_i n_j + \sum_{i=1}^M V_{\text{ext},i} n_i, \quad (8)$$

where  $\langle ij \rangle$  denotes nearest-neighbor sites only,  $M$  is the total number of sites in the pore-reservoir system,  $n_i (= 1$  or  $0)$  specifies the occupancy of the site  $i$ , and  $V_{\text{ext},i}$  is the external potential felt at site  $i$ . The external potential due to a single wall in the case of the slitlike pore was the integrated 9-3 Lennard-Jones potential, which is given by

$$\Phi(x) = \frac{2\pi\rho^*\epsilon}{3} \left[ \frac{2}{15} \left( \frac{\sigma}{x} \right)^9 - \left( \frac{\sigma}{x} \right)^{12} \right], \quad (9)$$

where  $x$  is the distance from the wall,  $\rho^* = \rho_w \sigma_{wf}^3$  is the reduced wall density and  $\sigma$  and  $\epsilon$  denote the lattice spacing and potential well depth, respectively. Note that the parameter  $\epsilon$  used in Eq. (9) to account for wall-fluid interaction is identical to that which appears in Eq. (8) to account for fluid-fluid interaction. In all our calculations we have set  $\rho^*$  equal to unity. By the superposition of the potentials from the two parallel walls a particle at a distance  $x$  from one wall feels the pore potential

$$V_{\text{pore}}(x_i) = \Phi(x_i) + \Phi(L_x - x_i + \sigma), \quad (10)$$

where  $L_x$  is the distance between the two walls.

As in the case of the cylindrical pore we superimposed hard walls on the slitlike pore to simulate the bulk fluid near the pore ends. The pore system (i.e., pore and reservoirs together), which we refer to as a finite slitlike pore, is shown in Fig. 1(b). Periodic boundary conditions were applied in both  $z$  and  $y$  directions. As in the case of the cylindrical pore, the external potential varies with  $z$  as

$$V_{\text{ext},i}(x_i) = V_{\text{pore}}(x_i)\Theta(z-z_1)\Theta(z_2-z). \quad (11)$$

The chemical potential at bulk saturation for the lattice gas model is independent of temperature and equal to  $3\epsilon$ . The critical temperature for the simple cubic lattice is  $k_B T_c / \epsilon = 1.1279$ .<sup>17</sup>

The lattice gas model in the grand ensemble is isomorphic with the magnetic spin Ising model in the canonical ensemble. Thus, simulations can be performed either in Ising spin-flip fashion or alternatively in the GCMC fashion. We used the GCMC method to simulate the slitlike pore adsorption isotherms. Briefly, each MC cycle consists of an attempted reversal of the state of each site, i.e., occupied site to unoccupied (destruction move) or vice versa (creation move), with a probability of acceptance given by<sup>18</sup>

$$\min \left[ 1, \exp \left[ + \epsilon \beta (\Delta n_i) \sum_j n_j + \beta \Delta n_i (\mu - V_{\text{ext},i}) \right] \right];$$

$$\Delta n_i = n_i^{\text{new}} - n_i^{\text{old}}. \quad (12)$$

Note that the lattice gas simulation consists entirely of destruction and creation moves and thus differs slightly from the typical GCMC for continuous fluids which includes shuffle moves as well. The argument here is that in a lattice a shuffle can be viewed as a composite step, namely, a destruction followed by a creation, and so there is no need for any shuffle moves.

On the other hand, the NVT simulation performed for the location of the transition chemical potential, was carried out in a manner similar to that for continuous fluids. Namely, each MC step consists of a destruction of an occupied site and an attempted creation to a randomly picked site. If the latter site is occupied the step is rejected; otherwise, it is accepted with probability  $\min\{1, \exp[-\beta(\Delta U_d + \Delta U_c)]\}$  where  $\Delta U_d$  and  $\Delta U_c$  are the energy differences during the first and second part of the move. After  $N$  MC steps, which constitute one MC sweep, the density of each site and the total energy accumulators are updated. The implementation of the PDT provides the means for the calculation of the coexistence chemical potential. Briefly, at the end of each MC sweep, a test particle is created in every unoccupied cell in the pore and the resulting factor  $\exp(-\beta\Psi)$  is accumulated. Occupied sites merely contribute zero to the average since  $\Psi = \infty$  for a creation of a particle in an occupied site. However, it is obvious that the normalized average is to be taken over *all* sites in the probe volume. As our probe volume we set the volume of the pore itself, excluding the sites in the reservoirs.

### III. RESULTS AND DISCUSSION

#### A. Cylindrical pores

We studied capillary condensation of fluid in cylindrical pores of finite length  $L_z = 10\sigma$  and  $L_z = 20\sigma$  using a hard wall section of  $H_z = 10\sigma$  on both pore ends. Periodic boundary conditions were applied to the whole system of pore reservoirs in the axial direction. The radius of the pore for each simulation was  $R = 5\sigma$ . The reduced temperature was  $k_B T / \epsilon = 0.7$ , which corresponds to  $T/T_c = 0.631$ , (i.e.,  $k_B T_c / \epsilon \approx 1.1$ ).

Using the hard wall section in our simulation for a pore of  $L_z = 10\sigma$  we obtained the hysteresis curve shown in Fig. 2(a). Here we plot the average number of particles, between  $z_1$  and  $z_2$ . The location of the phase transition is also indicated in Fig. 2. As can be seen from the data, the adsorption branch for a finite sized pore is extended to higher values of  $\mu^{\text{conf}}$  and the number of particles inside the finite pore is lower than that in a PBC pore of the same size (Table I). The novel feature of the addition of the reservoirs to the pores is most evident in the desorption branch. As  $\mu^{\text{conf}}$  is lowered,  $N$  falls substantially below the PBC desorption branch. A further decrease of  $\mu^{\text{conf}}$  produces an abrupt decrease in the number of particles and the pore finally empties at  $\mu^{\text{conf}}/\epsilon = -4.085$  compared to  $-4.361$  for the infinite pore. The hysteresis loop produced in this

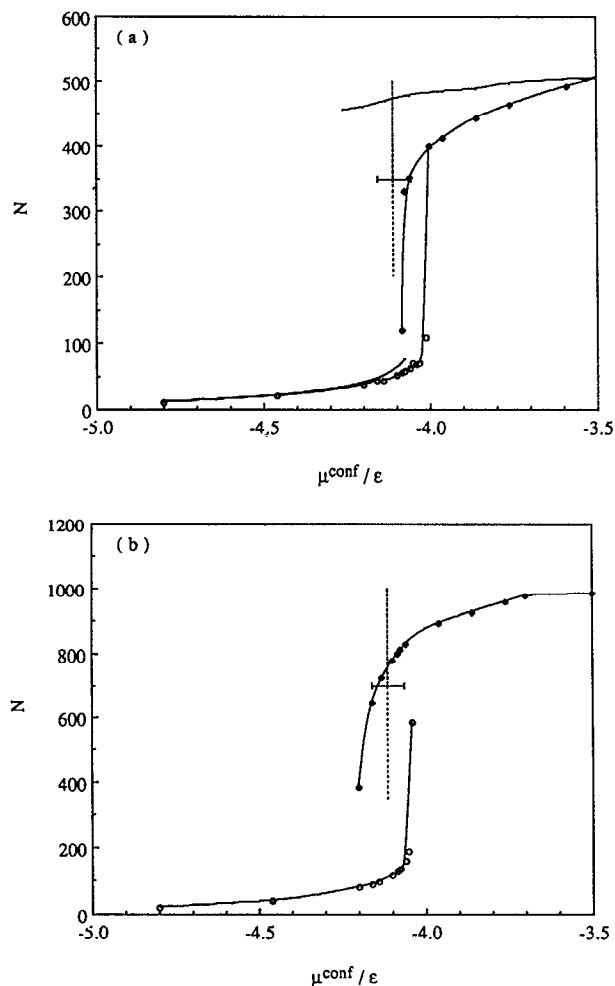


FIG. 2. Adsorption-desorption isotherms for cylindrical pores of varying lengths. (a)  $L_z = 10\sigma$ . The average number of particles in the pore only,  $N$ , is plotted vs  $\mu^{\text{conf}}/\epsilon$  [see Eq. (6)]. The symbols  $\circ$  and  $\diamond$  represent points along the adsorption and desorption branch, respectively, and interpolation curves are drawn. The solid curves without symbols depict the hysteresis loop observed for a PBC pore. The phase transition location is indicated by the dashed-dotted line along with the associated standard error in  $\mu^{\text{conf}}/\epsilon$ . (b)  $L_z = 20\sigma$ .

case is in qualitative agreement with the major features of adsorption hysteresis observed in experiments performed with a well-defined porous medium.<sup>3</sup> In particular, sharp capillary effects are present, thus producing a sharp hysteretic region, and no canted desorption isotherm is observed.

To address questions regarding the extent of the effect of pore ends on the location and the shape of the hysteresis loop and the sensitivity of the isotherm to the actual pore length as in a PBC pore, we studied hysteresis in a pore of  $L_z = 20\sigma$ . The results of this simulation are shown in Fig. 2(b). We conclude that the pore length does not appear to affect the main features of the hysteresis loop, although one may observe a shift of the hysteresis loop to lower values of  $\mu$  as the pore length increases. In particular, by increasing the pore length we expect the adsorption branch to decrease and finally fall on top of the PBC adsorption branch

TABLE I. (a) GCMC simulation results for cylindrical pore of length  $L_z=10\sigma$ . (b) GCMC simulation results for cylindrical pore of length  $L_z=20\sigma$ .

$\mu^{\text{conf}}/\epsilon^a$	$N^b$	$U/N\epsilon^b$	$N$	$N_{\text{pore}}$	$\Delta N^2/N^2$	$U/N\epsilon$
(a)						
-4.800	10.8	-2.73	12.32	10.63	1.21	-2.43
-4.461	20.8	-2.87	22.53	19.74	1.43	-2.57
-4.200	41.3	-3.19	41.75	37.64	2.25	-2.86
-4.161			47.97	43.60	2.57	-2.95
-4.141			48.70	44.19	2.33	-2.94
-4.100	63.4	-3.45	56.54	51.74	2.46	-3.04
-4.085			61.33	56.39	3.03	-3.11
-4.075	75.5	-3.58	62.32	57.32	2.75	-3.11
-4.061	474.1	-5.48	66.76	61.62	3.10	-3.17
-4.051			74.47	69.28	3.85	-3.28
-4.041			73.56	68.22	3.34	-3.24
-4.031			76.29	70.89	3.89	-3.27
-4.011			113.99	108.35	20.09	-3.72
-4.000			407.59	399.91	0.59	-4.98
-3.588			528.79	491.81	0.30	-5.17
-3.761	496.5	-5.66	480.66	463.60	0.35	-5.13
-3.861	488.2	-5.59	454.01	442.13	0.45	-5.09
-3.961	484.2	-5.56	420.55	412.02	0.92	-5.01
-4.061	478.1	-5.51	357.17	351.24	1.32	-4.84
-4.075			335.42	329.81	1.49	-4.77
-4.085			123.48	118.45	91.11	-4.11
-4.161	469.3	-5.44				
-4.261	459.4	-5.35				
-4.361	454.6	-5.31				
(b)						
$\mu^{\text{conf}}/\epsilon$	$N$	$N_{\text{pore}}$	$\Delta N^2/N^2$	$U/N\epsilon$		
-4.800	23.14	21.46	1.21	-2.61		
-4.461	43.52	40.72	1.43	-2.76		
-4.200	84.17	80.05	2.25	-3.06		
-4.161	94.00	89.63	2.57	-3.11		
-4.141	102.22	97.67	2.33	-3.17		
-4.100	123.15	118.33	3.22	-3.30		
-4.085	132.01	127.03	4.19	-3.35		
-4.075	139.91	134.88	5.30	-3.40		
-4.061	164.64	159.50	8.42	-3.55		
-4.051	194.24	189.02	21.28	-3.72		
-4.041	591.26	585.54	121.12	-4.95		
-3.500	1014.27	983.02	0.25	-5.40		
-3.700	1000.35	976.39	0.20	-5.43		
-3.761	974.09	955.99	0.20	-5.38		
-3.861	936.05	924.75	0.20	-5.33		
-3.961	899.71	891.49	0.26	-5.31		
-4.061	832.84	827.01	0.38	-5.22		
-4.075	815.19	809.42	0.45	-5.20		
-4.085	802.91	797.14	1.68	-5.17		
-4.100	784.65	779.36	0.90	-5.16		
-4.141	725.83	721.01	1.35	-5.10		
-4.161	651.00	646.49	4.57	-5.03		
-4.200	390.70	386.52	154.46	-4.80		

<sup>a</sup>See text, Eq. (6).

<sup>b</sup>PBC results (Ref. 6)  $U$  denotes the potential energy.

while the desorption branch will curve and follow the true transition.

A check on the GCMC results is provided by the measured bulk density in the reservoir, which should match the density implied by the chemical potential in conjunction with the equation of state. The bulk density was calculated

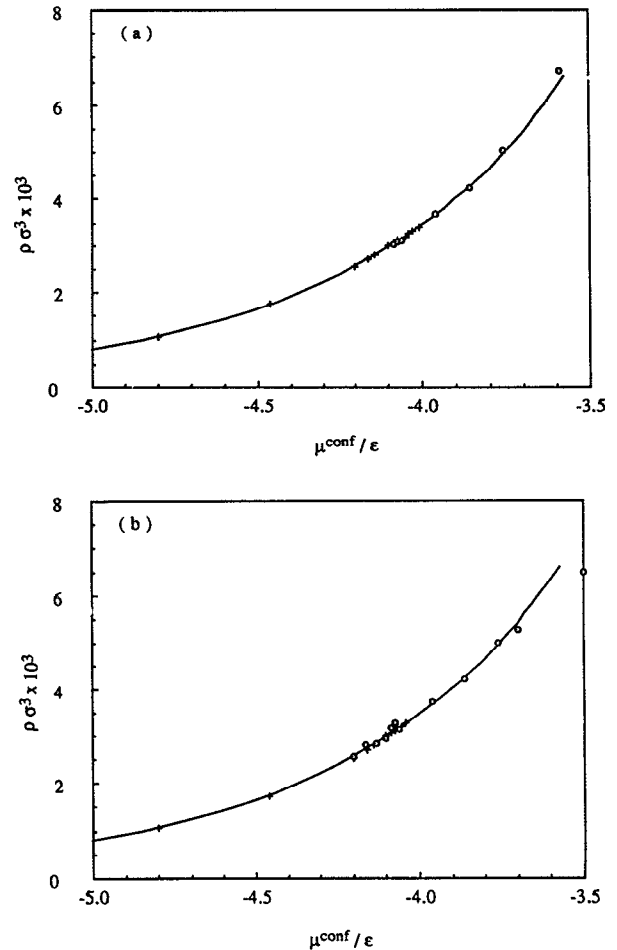


FIG. 3. Average density in reservoirs (— virial expansion, + adsorption and ○ desorption data) for cylindrical pores of length (a)  $L_z=10\sigma$  and (b)  $L_z=20\sigma$ .

by inverting the truncated virial equation of state. The virial expansion of the chemical potential is given by

$$\beta\mu^{\text{conf}} = \ln \rho\sigma^3 + \sum_{n=1}^{\infty} \frac{n+1}{n} B_{n+1}\rho^n, \quad (13)$$

where  $B_i$  is the  $i$ th virial coefficient. We have checked that for the present range of bulk densities the virial equation can be truncated at the second virial coefficient,  $B_2 = -8.133\ 206\sigma^3$  for cut-and-shifted LJ fluid at  $r_c=2.5\sigma$  and for  $kT/\epsilon=0.7$ . In Fig. 3 the density is plotted vs  $\mu^{\text{conf}}/\epsilon$ . We define the bulk fluid density to be the average density of the reservoir fluid which is at least  $5\sigma$ , i.e., twice the cutoff distance, away from the pore ends. Integrating the axial density  $\rho(z)$  along that region, ensures the absence of correlations with the fluid inside the pore. The bulk fluid density from our simulations and from the virial equation of state for a given value of the chemical potential clearly are in excellent agreement.

Another check on the consistency of the simulation results is provided by the PDT for the inhomogeneous fluids [see Eq. (7)]. The relation between the preset  $\mu^{\text{conf}}$  and the one calculated using the PDT is depicted in Fig. 4. The excessive noise which is mainly in the desorption data where the density inside the pore is high, was traced to be

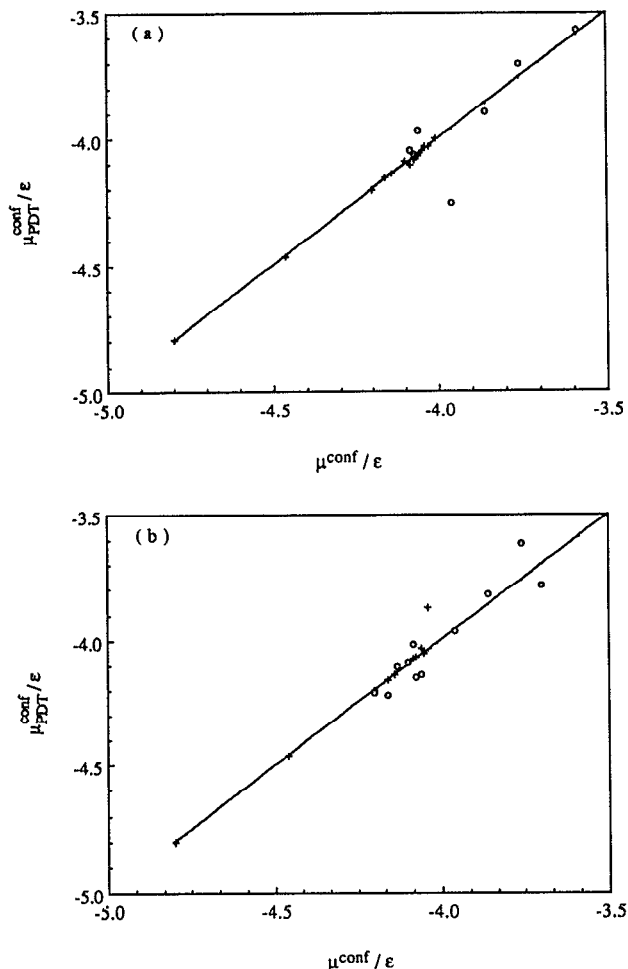


FIG. 4. Comparison of PDT results with the preset chemical potential for cylindrical pores of two different lengths. The solid line depicts the preset  $\mu^{\text{conf}}/\epsilon$ . (a)  $L_z=10\sigma$  and (b)  $L_z=20\sigma$ .

TABLE II. Phase coexistence data.

$n^a$	$\mu_1$	st. er <sub>1</sub>	$\mu_2$	st. er <sub>2</sub>	$\mu_3$	st. er <sub>3</sub>	$\mu_4$	st. er <sub>4</sub>	$\mu_5$	st. er <sub>5</sub>
10	-3.852	0.160	-4.101	0.097	-4.037	0.126	-3.994	0.076	-4.147	0.037
20	-3.765	0.137	-4.025	0.100	-4.015	0.090	-3.960	0.070	-4.128	0.046
30	-3.708	0.119	-3.937	0.101	-4.008	0.075	-3.914	0.073	-4.119	0.043
			$n^b$	$\mu$	st. er					
			10	-4.106	0.049					
			20	-4.095	0.045					
			30	-4.090	0.039					
$n^c$	$\mu_1$	st. er <sub>1</sub>	$\mu_2$	st. er <sub>2</sub>	$\mu_3$	st. er <sub>3</sub>	$\mu_4$	st. er <sub>4</sub>	$\mu_5$	st. er <sub>5</sub>
10	-3.747	0.175	-3.899	0.095	-3.967	0.110	-4.222	0.070	-4.083	0.032
20	-3.525	0.179	-3.882	0.074	-3.938	0.089	-4.192	0.068	-4.069	0.040
30	-3.329	0.170	-3.839	0.078	-3.867	0.084	-4.110	0.088	-4.063	0.035
			$n^d$	$\mu$	st. er					
			10	-4.112	0.048					
			20	-4.105	0.040					
			30	-4.090	0.042					

<sup>a</sup> $L_z=10\sigma$ ,  $\mu_i$  denotes the configurational  $\mu$  in probe volume  $i$  and the standard error (st. er) associated with it.

<sup>b</sup> $L_z=10\sigma$ , the coexistence configurational  $\mu$  over the probe volume of  $R=4.3\sigma$ .

<sup>c</sup> $L_z=20\sigma$ , same as footnote (a).

<sup>d</sup> $L_z=20\sigma$ , same as in footnote (b).

due to the choice of probe volume, namely  $R_{\text{probe}}=5\sigma$ , which allows sampling too close to the walls.

The location of the phase transition was determined by performing an NVT simulation on the pore systems ( $N=350$  for  $L_z=10\sigma$  and  $N=700$  for  $L_z=20\sigma$ ). The NVT simulations consisted of  $12 \times 10^6$  MC steps for each pore length. Subaverages of  $\rho$  and  $\langle \exp[-(\beta\Psi)] \rangle$  in a probe volume of radius  $R_{\text{NVT}}=4.3\sigma$  were taken every 10 000 MC steps. In order to estimate the standard error to the chemical potential, the averages were broken up into subaverages of different length thus producing samples of different size. As the sample size increases the standard deviation should approach a constant value from below.<sup>19</sup> The division of the probe volume into five concentric subcells yielded the results presented in Table II. We find that the chemical potential in each subcell is constant within the standard error with the exception of that in subcell 1. The spuriously high value in subcell 1 is due to poor statistics due to the small number of created particles in the particular subcell. Normalization of  $(\mu^{\text{conf}}/\epsilon)_i$  with the volume of subcell  $i$  and taking their normalized average yields a value close to that calculated in the total probe volume. The coexistence chemical potential calculated by insertion of test particles into the total probe volume for a pore of length  $L_z=10\sigma$  is found to be  $\mu^{\text{conf}}/\epsilon = -4.106 \pm 0.049$  and for  $L_z=20\sigma$  we obtained  $\mu^{\text{conf}}/\epsilon = -4.112 \pm 0.048$ . Previous PBC calculations (MC and MD) yielded  $\mu^{\text{conf}}/\epsilon = -4.16$  and  $-4.14$ , respectively.<sup>6,7</sup> Although one does expect a slight shift in  $\mu_{\text{coex}}$  as  $L_z$  increases,<sup>10</sup> this shift is too small to be picked up by the simulations reported here. We point out though, that it can be measured in the lattice gas simulation results (see following section).

The radial density profiles of the fluid inside the pore,

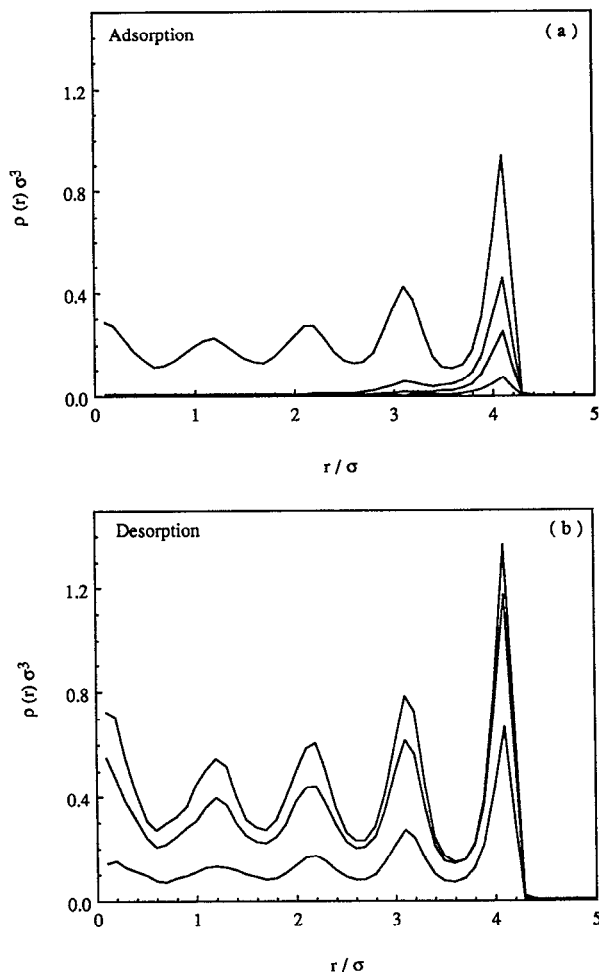


FIG. 5. Radial density profiles, (defined in the text), during: (a) adsorption ( $\mu^{\text{conf}}/\epsilon = -4.8, -4.2, -4.061, -4.041$ ) and during (b) desorption ( $\mu^{\text{conf}}/\epsilon = -3.5, -4.061, -4.2$ ) for a cylindrical pore of length  $L_z = 20\sigma$ .

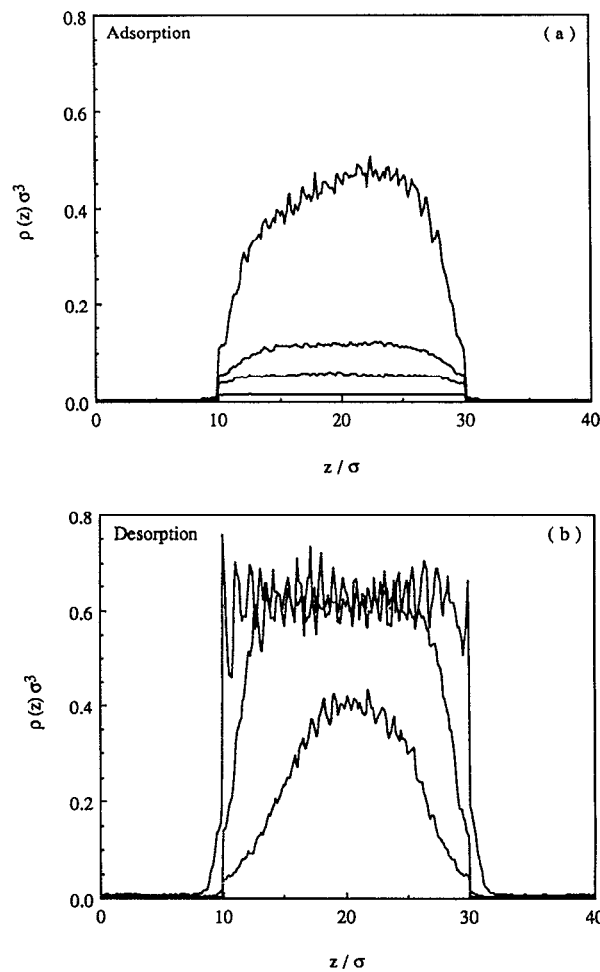


FIG. 6. Axial density profiles, (defined in the text), during: (a) adsorption ( $\mu^{\text{conf}}/\epsilon = -4.8, -4.2, -4.061, -4.041$ ) and during (b) desorption ( $\mu^{\text{conf}}/\epsilon = -3.5, -4.061, -4.2$ ) for a cylindrical pore of length  $L_z = 20\sigma$ .

$\rho(r) = 1/z_{\text{tot}} \int_0^{z_{\text{tot}}} dz \rho(r, z)$  are plotted in Fig. 5. For states along the adsorption branch  $\rho(r)$  exhibits a pronounced peak approximately  $1\sigma$  away from the wall which corresponds to the formation of a monolayer of dense fluid on the wall, as continuously assumed by macroscopic theories. A further increase of the chemical potential causes the formation of a second peak at a distance approximately  $1\sigma$  from the first peak which persists until the gas ultimately condenses. This results in a density profile which is a linear combination of the profiles that describe states along the adsorption and the desorption branches. Along the desorption branch and for high values of  $\mu^{\text{conf}}$  five distinct peaks are present illustrating the packing effects. The increased height of the center peak is due to the cylindrical shape in combination with the particular radius. As noted by Peterson and Gubbins this increased density no longer exists for a pore with radius of a noninteger value.<sup>6</sup>

The axial density profiles,  $\rho(z) = 2/R^2 \int_0^R dr r \rho(r, z)$  shown in Fig. 6 further illustrate the formation of a thin monolayer during adsorption. A new feature that can be detected is the effect of the pore ends on the structure of the fluid inside the pore. Namely, the density profile exhib-

its a tiny cusp near the ends of the pore due to the presence of the bulk fluid and the fact that the external pore potential is discontinuous [see Eq. (5)]. Along the desorption branch, at relatively high chemical potential the liquid inside the pore causes the condensation of the bulk gas in the reservoir close to the pore ends which is indicated by an accumulation in that region. For states along the desorption branch at lower  $\mu^{\text{conf}}$ , the density profiles indicate the formation of a meniscus near the pore ends. As the chemical potential is further reduced, the plateau in the center of the pore decreases.

To present a more detailed picture of the formation of the menisci we plot the  $\rho(r, z)$  density for states along the adsorption and the desorption branches in Fig. 7. The mirror image of  $\rho(r, z)$  along the pore axis was added to help visualize the structure of the fluid in the pore system. The result resembles a cross-sectional view of the cylinder. To increase the contrast we used a shading procedure whereby the shade of each point is proportional to a hyperbolic tangent of the average density at the particular  $r$  and  $z$ . The formation of the first monolayer next to the walls appears as an almost solid black line and an increase in  $\mu^{\text{conf}}$  leads

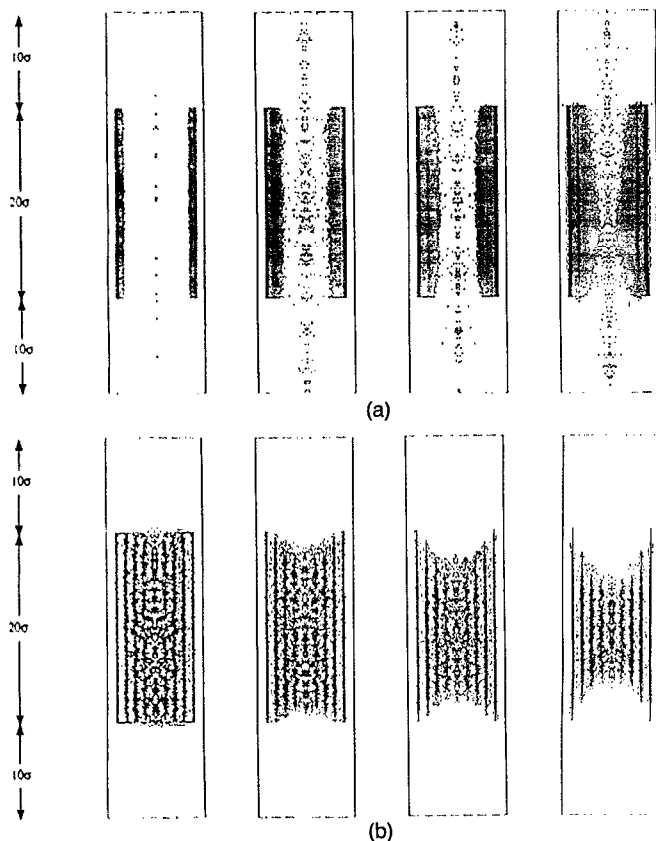


FIG. 7. Average  $\rho(r,z)$  profiles during: (a) adsorption ( $\mu^{\text{conf}}/\epsilon = -4.5, -4.2, -4.085, -4.051$ ) and (b) desorption ( $\mu^{\text{conf}}/\epsilon = -3.5, -3.861, -4.131, -4.161$ ) for cylindrical pore of length  $L_z = 20\sigma$ . The mirror image of  $\rho(r,z)$  along the cylindrical axis has been taken to help the visualization of the fluid structure. Thus, the picture resembles an axial cylindrical cross section.

to the appearance of a second dark line. A further increase in  $\mu^{\text{conf}}$  leads to the formation of a wavelike distortion which is depicted by the cylindrical films bulging towards the axis of the pore and eventually creating a region of high density along the pore axis. One may also observe that while in the shorter pore the high density region is located near the center of the pore, in the larger pore it takes place off center. For states along the desorption branch, (high  $\mu^{\text{conf}}$ ), a convex gas-liquid interface appears, which reflects the liquid bulging out at the pore ends. Upon lowering  $\mu^{\text{conf}}$  concave hemispherical menisci start to develop at the pore ends. Further lowering of  $\mu^{\text{conf}}$  causes the menisci to recede to a point where they see each other and the fluctuations are then sufficient to cause a jump from the metastable liquidlike phase to the stable gaslike phase.

In a periodic pore, with no end effects, an increase in the fluctuations in  $N$  is the precursor for the formation of a droplet during adsorption. In our system, the bulging process is affected by the presence of pore ends, since the pore ends pin and induce the bulging. As the pore length increases, the end effects, which are restricted to the immediate neighborhood of the pore ends, become smaller. Thus, as the pore length increases the adsorption branch moves closer to that of the periodic pore, the end effects becoming negligible. On the other hand, during desorption, in a periodic pore, a substantial amount of undersaturation

is needed for the formation of the first bubble. In contrast, in our system, an interface between the bulk fluid, i.e., reservoir fluid, and the adsorbed fluid (liquid) exists in the shape of a convex (concave) meniscus at high  $\mu^{\text{conf}}$  (low  $\mu^{\text{conf}}$ ) and a retracting hemispherical meniscus serves as the mechanism for the emptying of the pore. Thus, for the desorption branches, one no longer finds that the pore-end effects are negligible with increasing length of the pore. As mentioned before, the desorption branch for a finite sized pore also exhibits a rounded knee which is absent in the case of the periodic pore where no meniscus is present and where, as soon as the fluctuations needed to form a bubble are acquired, the system immediately jumps from a liquidlike phase to a gaslike phase. Thus, the observation of a rounded knee is a direct consequence of the presence of pore ends and is not due to the finite size of the pore. The shape of the hysteresis curve remains unchanged as the pore length increases, but it shifts to slightly lower values of  $\mu^{\text{conf}}$ .

## B. Slitlike pores. Lattice gas simulations

We used the lattice gas model to simulate capillary condensation of a fluid inside a slitlike pore. We performed simulations on a PBC pore of size  $10 \times 10 \times 40$  sites and on finite sized pores with open ends of lengths 20, 40, and 80. For the latter the wall-to-wall distance was 10, the length along the  $y$  direction was 5 and each hard wall was of height 10. The reduced temperature  $k_B T/\epsilon$  was 0.6, which corresponds to  $T/T_c = 0.532$ .

The average density of occupied cells (or equivalently particles) between  $z_1$  and  $z_2$  [see Fig. 1(b)] vs  $\mu/\epsilon$  is presented in Fig. 8. The adsorption isotherm for the infinite pore produces evidence of layering as well as a hysteresis loop around the capillary condensation transition, although one does not expect to see true layering transitions at this relatively high temperature  $k_B T/\epsilon = 0.6$  (the 2D critical temperature being 0.567). Thus the (0,1) layering is followed by a prolonged plateau with increasing chemical potential and a (1,2) layering which is followed by a more steeply increasing branch which eventually ends due to the capillary condensation of the adsorbed fluid. The desorption branch, on the other hand, extends longer into the liquidlike phase, thus producing a hysteresis loop, and drops off with a large jump to a configuration of only one adsorbed layer and then follows the adsorption branch. The simulations of pores with open ends produced adsorption isotherms which exhibit all the above-mentioned features with the exception that the desorption branch is much shorter and appears rounded. It is also interesting to note that the jump from the liquidlike to the stable gaslike state results in a configuration of two layers instead of one. The adsorption branch for a finite pore is virtually the same as that of the PBC pore except in the region of two-layer profiles. In this region, the finite size pore curves lie below the PBC curve. The desorption branches apart from appearing rounded, also shift to lower values of  $\mu$  with increasing pore length. Therefore, a widening of the hysteresis loop occurs.

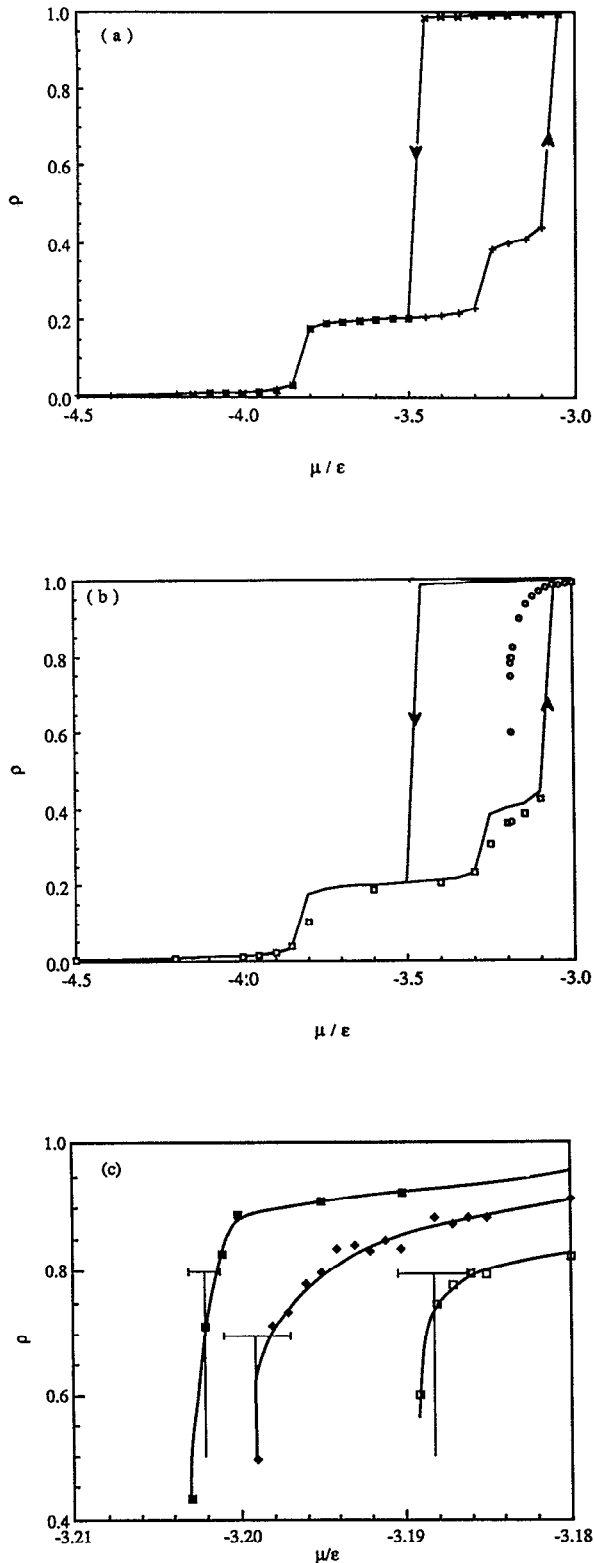


FIG. 8. Adsorption-desorption hysteresis: (a) for a slitlike pore (PBC) of size  $10 \times 10 \times 40$  sites. Here, the average number density,  $\rho$ , inside the pore is plotted vs  $\mu/\epsilon$ . (+ denote adsorption and  $\times$  desorption points. Interpolation between the above points produces the solid curves.) (b) Comparison of the PBC pore hysteresis with a finite size slitlike pore of size  $10 \times 5 \times 40$ . (c) Comparison of desorption curves for finite pores of length 20, 40, and 80 (symbols  $\square$ ,  $\blacklozenge$ , and  $\blacksquare$ , respectively). The location of the phase coexistence  $\mu/\epsilon$  is depicted by the vertical solid lines along with the associated standard errors.

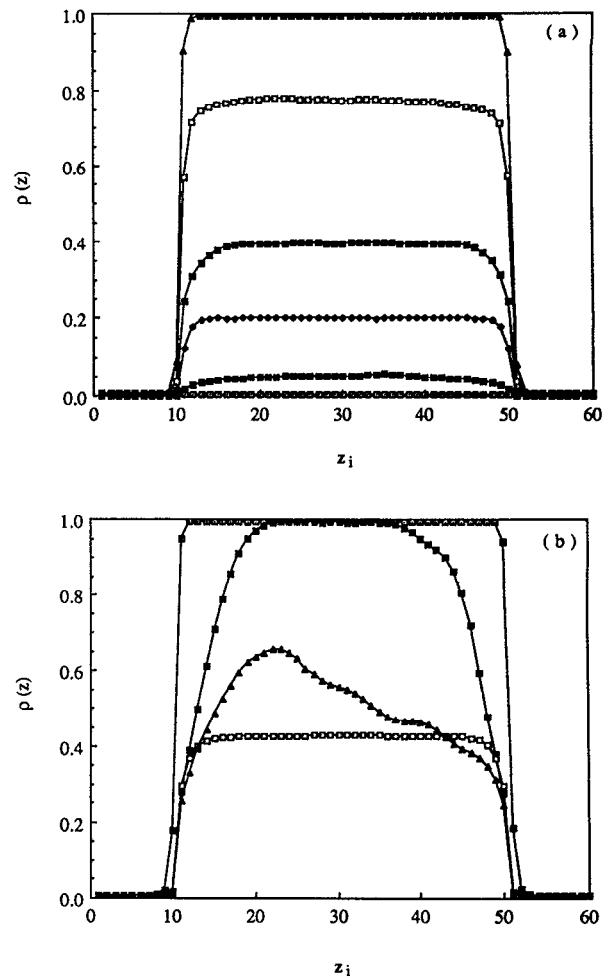


FIG. 9.  $\rho(z)$  density profiles, (defined in the text), during: (a) adsorption ( $\mu/\epsilon = -4.5, -3.85, -3.6, -3.2, -3.1, -3.05$ ) and (b) desorption ( $\mu/\epsilon = -3.0, -3.193, -3.199, -3.2$ ) for a slitlike pore of length  $L_z = 40$ .

The simulation results for the location of the first order transition (from an NVT simulation and applying the PDT) are averages over 50 000 MC sweeps each cycle consisting of  $N$  MC steps. Thus, for the PBC pore the transition was located at  $\mu/\epsilon = -3.203\ 82 \pm 0.000\ 2$ , for the pore of length 20 the phase coexistence was located at  $\mu/\epsilon = -3.188\ 174 \pm 0.002\ 148$  using  $N = 800$ , for the pore of length 40 at  $\mu/\epsilon = -3.199\ 0 \pm 0.001\ 947$  using  $N = 1400$  and for the pore of length 80 at  $\mu/\epsilon = -3.202\ 038 \pm 0.000\ 925$  using  $N = 3200$ .

The  $z$ -direction density profiles,  $\rho(z_m) = 1/L_x L_y \sum_{k=1}^{L_x} \sum_{l=1}^{L_y} \langle n_{k,l,m} \rangle$ , for different values of  $\mu$  during adsorption and desorption are presented in Fig. 9. The formation of the first and second layers are evident in these graphs. As in the case of the continuous fluid the bulging of the dense gaslike fluid occurs at the center of the pore, shown by the lower density at the end bins of each pore compared to an almost constant density in the middle of the pore. The density profiles which correspond to states along the desorption branch show clear evidence of the formation of menisci at the pore ends and the jump to a two-layer configuration is also evident. A skewed density

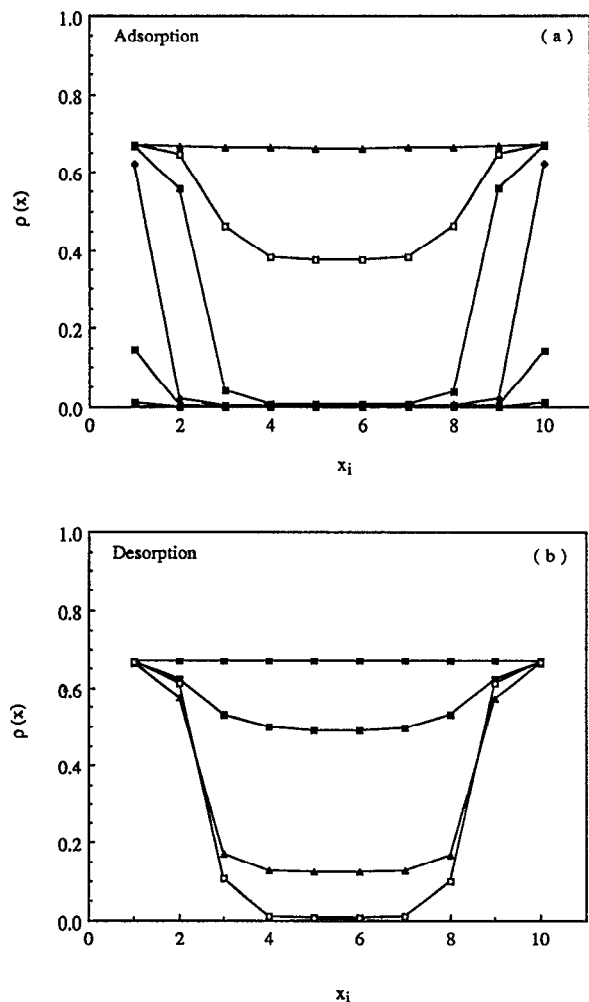


FIG. 10.  $\rho(x)$  density profiles, (defined in the text), during: (a) adsorption ( $\mu/\epsilon = -4.5, -3.85, -3.6, -3.2, -3.1, -3.05$ ) and (b) desorption ( $\mu/\epsilon = -3.0, -3.193, -3.199, -3.2$ ) for a slitlike pore of length  $L_z = 40$ .

profile shows that the fluid apparently strongly fluctuates between a three- and a two-layer configuration. A small decrease of the chemical potential ( $\Delta\mu/\epsilon = -0.001$ ) causes the system to finally stabilize in a two-layer configuration.

The same conclusions with regard to the mechanism of capillary adsorption can be drawn from the  $\rho(x_i)$  density profiles,  $\rho(x_k) = 1/L_y L_z \sum_{l=1}^{L_y} \sum_{m=1}^{L_z} \langle n_{k,l,m} \rangle$  (see Fig. 10), namely, that the adsorption mechanism consists of three steps, the formation of the first layer, of the second layer, and capillary condensation. The desorption mechanism, on the other hand, involves the formation and the retraction of a meniscus. It can also be seen that the thickness of the unperturbed layers on the walls while the meniscus is formed equals two.

Thus, the implementation of the reservoirs at the pore ends produces a hysteresis loop, which is in excellent agreement with the results of Marini Bettolo Marconi and van Swol<sup>10</sup> and in qualitative agreement with the results presented for continuous fluids in cylindrical pores.

#### IV. CONCLUSIONS

The behavior of the continuous fluid in a cylindrical pore with open ends and that of a discrete fluid in a slitlike pore with open ends are very similar with regard to the adsorption hysteresis. The mechanism for the adsorption involves the formation of a monolayer of dense gas on the walls followed by other layers and the formation of density fluctuations along the pore axis ultimately leading to capillary condensation. Desorption starts with the formation of menisci at the pore ends. The menisci recede, as the chemical potential is lowered, to the point where they interact with each other causing the system to jump to the more stable gaslike configuration.

The simulation of pores with open ends provides a hysteresis loop which is qualitatively different from the simulation results obtained for periodic pores. Namely, the PBC system produces an artificially extended desorption branch. This feature can be explained by the presence of nucleation barriers. When periodic conditions are replaced by open ends one apparently overcomes the nucleation barrier for desorption but leaves the one for adsorption intact. Thus, the pore ends help to break the symmetry for the desorption but not for the adsorption and therefore hysteresis persists. One way to overcome the adsorption barrier is to close off one end<sup>10</sup> in which case hysteresis likely disappears.

The effect of the pore ends on the shape of hysteresis is reflected in a rounded knee followed by sharp decline of the desorption branch very close to the phase transition. The effect of the finite pore length itself is merely a shift of the hysteresis loop along with the transition to lower chemical potentials, as the pore length is increased. Thus, we conclude that the fluctuations, which are not taken into account in the mean field DFT,<sup>10</sup> do not have any qualitative effect on the hysteric behavior of the fluid inside a narrow pore.

The hysteresis loop is entirely due to the prolonged extent of the gaslike phase since the desorption virtually occurs at the chemical potential of the phase transition. One may therefore expect that for a pore of  $L_z \rightarrow \infty$  with open ends the adsorption branch will be identical with that of a PBC pore, while the desorption branch will persist to exhibit the rounded knee which will occur at the phase coexistence chemical potential.

Having shown, via a self-consistent study, that hysteresis exists in single pores, a challenge will be to combine the two complimentary approaches, namely single pore hysteresis and hysteresis due to pore blocking effects.

Our preliminary DFT results show that both single pore hysteresis and hysteresis connected with pore blocking in systems of interconnected slitlike pores of widely different wall-to-wall distance exist. In general, pore blocking effects are present during desorption while the adsorption branches are merely a superposition of the adsorption branches observed for the respective individual pores, although the topology of the system under consideration is an important factor to the observance of a particular type of hysteresis loop. For example, a system of not widely different interconnected pores exhibits a hysteresis loop

similar to a single pore hysteresis. A shortcoming of DFT is that although it detects the equilibrium and metastable states it does not allow for diffusion to be the rate determining step of the adsorption process, and thus one cannot calculate the time scales involved to reach equilibrium. Since hysteresis due to pore blocking implies diffusion limitations mainly during desorption, to overcome the DFT drawback we have developed a new MD method in the grand canonical (GCMD),<sup>20</sup> which allows diffusion of particles in and out the pore network and the observation of the time scales involved for one to attain the equilibrium states.

#### ACKNOWLEDGMENT

The authors would like to thank Brian K. Peterson for many useful discussions.

- <sup>1</sup>S. J. Gregg and K. S. W. Sing, *Adsorption, Surface Area and Porosity* (Academic, New York, 1982).
- <sup>2</sup>G. Mason, *J. Colloid. Interface Sci.* **88**, 36 (1982); *Proc. R. Soc. London, Ser. A* **390**, 47 (1983).
- <sup>3</sup>D. D. Awshalom, J. Warnock, and M. W. Shaffer, *Phys. Rev. Lett.* **57**, 1607 (1987).
- <sup>4</sup>R. Evans, U. Marini Bettolo Marconi, and P. Tarazona, *J. Chem. Phys.* **84**, 2376 (1986); *J. Chem. Soc. Faraday Trans. 2* **82**, 1763 (1986).
- <sup>5</sup>P. C. Ball and R. Evans, *Mol. Phys.* **63**, 159 (1988).
- <sup>6</sup>B. K. Peterson and K. E. Gubbins, *Mol. Phys.* **62**, 215 (1987).
- <sup>7</sup>G. S. Heffelfinger, F. B. van Swol, and K. E. Gubbins, *Mol. Phys.* **61**, 1381 (1987); *J. Chem. Phys.* **89**, 5202 (1988).
- <sup>8</sup>M. Schoen, Jr., C. L. Rhykerd, J. H. Cushman, and D. J. Diestler, *Mol. Phys.* **66**, 1171 (1989).
- <sup>9</sup>S. K. Ma, *Statistical Mechanics* (World Scientific, Singapore, 1985); E. W. Montroll, in *Fluctuation Phenomena*, edited by J. L. Lebowitz (Elsevier Science, New York, 1979).
- <sup>10</sup>U. Marini Bettolo Marconi and F. B. van Swol, *Europhys. Lett.* **8**, 531 (1989); *Phys. Rev. A* **39**, 4109 (1989).
- <sup>11</sup>J. R. Henderson and F. B. van Swol, *Mol. Phys.* **56**, 1313 (1985).
- <sup>12</sup>D. J. Adams, *Mol. Phys.* **29**, 307 (1975).
- <sup>13</sup>B. Widom, *J. Chem. Phys.* **39**, 2808 (1963).
- <sup>14</sup>B. Widom, *J. Phys. Chem.* **86**, 869 (1982).
- <sup>15</sup>U. Heinbuch and J. Fischer, *Mol. Simul.* **1**, 109 (1987).
- <sup>16</sup>J. S. Rowlinson and B. Widom, *Molecular Theory of Capillarity* (Oxford University, New York, 1982).
- <sup>17</sup>G. S. Pawley, R. H. Swendsen, D. J. Wallace, and K. G. Wilson, *Phys. Rev. B* **29**, 4030 (1984).
- <sup>18</sup>D. A. Chesnut and Z. W. Salsburg, *J. Chem. Phys.* **38**, 2861 (1963).
- <sup>19</sup>M. P. Allen and D. J. Tildesley, *Computer Simulation of Liquids* (Oxford University, New York, 1987).
- <sup>20</sup>A. Papadopoulou, E. D. Becker, M. Lupkowski, and F. van Swol (to be submitted).